







RESEARCH ARTICLE | MARCH 17 2023

Shape design of an artificial pump-lung using high-resolution hemodynamic simulation with high-performance computing

Wei Chen (陈威) ; Hairong Zheng (郑海荣) ; Zhengzheng Yan (闫争争)  ;
Rongliang Chen (陈荣亮)  



Physics of Fluids 35, 031909 (2023)

<https://doi.org/10.1063/5.0140986>



View
Online



Export
Citation

CrossMark

Articles You May Be Interested In

Investigation of hemocompatibility and vortical structures for a centrifugal blood pump based on large-eddy simulation

Physics of Fluids (November 2022)

Hemodynamic analysis of carotid endarterectomy

Physics of Fluids (January 2023)

The erythrocyte destruction mechanism in non-physiological shear mechanical hemolysis

Physics of Fluids (November 2022)

Shape design of an artificial pump-lung using high-resolution hemodynamic simulation with high-performance computing

Cite as: Phys. Fluids **35**, 031909 (2023); doi: [10.1063/5.0140986](https://doi.org/10.1063/5.0140986)

Submitted: 2 January 2023 · Accepted: 23 February 2023 ·

Published Online: 17 March 2023







View Online



Export Citation



CrossMark

Wei Chen (陈威),^{1,a)}  Hairong Zheng (郑海荣),^{1,b)}  Zhengzheng Yan (闫争争),^{1,2,c)} 
and Rongliang Chen (陈荣亮)^{1,2,c)} 

AFFILIATIONS

¹Shenzhen Institutes of Advanced Technology, Chinese Academy of Sciences, Shenzhen 518055, Guangdong, China

²Shenzhen Key Laboratory for Exascale Engineering and Scientific Computing, Shenzhen 518055, Guangdong, China

^{a)}Electronic mail: iewnehc@mail.ustc.edu.cn

^{b)}Electronic mail: hr.zheng@siat.ac.cn

^{c)}Authors to whom correspondence should be addressed: zz.yan@siat.ac.cn and rl.chen@siat.ac.cn

ABSTRACT

Accurate and fast prediction of the hemodynamics of the artificial pump-lung is critical in the design process. In this study, a comprehensive computational framework, including a sliding mesh method, a coupled free flow and porous media flow model, a hemolysis prediction method, a $k - \omega$ shear stress transport turbulence model, and solution algorithms, is introduced to accurately predict the velocity field, pressure heads, and hemolysis. The framework is used to do the shape design of an artificial pump-lung on a supercomputer. High-resolution hemodynamics simulation results are obtained and analyzed, and the parallel performance of the algorithm is studied. The numerical results indicate that the proposed framework is capable of accurately predicting the velocity field, pressure heads, and hemolysis, and the performance of the designed artificial pump-lung meets the biocompatibility requirements. Additionally, the parallel performance results demonstrate the potential of the framework to efficiently perform the design of artificial pump-lungs using a large number of processors.

Published under an exclusive license by AIP Publishing. <https://doi.org/10.1063/5.0140986>

I. INTRODUCTION

Extracorporeal membrane oxygenation (ECMO) is a medical device that provides a short- and long-term gas exchange for patients with severe but potentially reversible respiratory and heart failure.¹ The device consists of a unique bundle of hollow fiber membranes known as an oxygenator, which exchanges oxygen and carbon dioxide, and a magnetically levitated centrifugal impeller pump. In a typical ECMO system, the venous blood is drawn from the patient's central vein, goes through the oxygenator, and is then reinserted into the iliac artery.²

In the past, ECMO design was primarily based on physical experimentation, which was time-consuming and costly, and also made it difficult to visualize and evaluate the hydrodynamics of the oxygenators due to their opacity. In contrast, computational fluid dynamics (CFD) provides a fast, flexible, intuitive, and accurate method for designing and optimizing the pump and oxygenator. Using CFD, one can gain insight into the device's performance and obtain data that

would be difficult to measure in the physical experiment, without having to produce costly prototypes.³ By using CFD, the need for experimental trial and error can be reduced. The design of a certain biomedical device can be achieved by comparing its performance against the defined objective functions.⁴

Existing CFD studies on ECMO devices can mainly be classified into three categories: analysis of the blood pump based on turbulence flow models, optimization of the hollow fiber membrane using various mathematical models, and study of the integrated pump-lung system using a model that couples the free flow and porous medium models. For the blood pump simulation, Puentener *et al.* conducted a comparative study of CFD simulations and *in vitro* hemolysis tests of a centrifugal blood pump with several variations, and obtained practical schemes for improving their biological compatibility.^{5,6} Fu *et al.* investigated the performance of a centrifugal pump using numerical simulation, hydraulic experiments, and *in vitro* hemolysis tests, and found that it has a good hemodynamic performance.⁷ Yang *et al.* optimized

the structural parameters of a conical axial maglev blood pump and predicted its hemolysis performance using CFD.⁸ Liu *et al.* studied the hemodynamic performance and the hemocompatibility of a centrifugal blood pump using the large-eddy simulation, and they compared several turbulence models.⁹ Good and Manning studied a Food and Drug Administration (FDA) benchmark centrifugal blood pump using a $k - \omega$ turbulence model and validated the simulation result using an experimental particle image velocimetry (PIV) database.¹⁰ They also compared the performance of Newtonian and viscoelastic blood models and found that there was a significant difference at low flow rates and pump impeller speeds. Ghadimi *et al.*¹¹ used a metamodel-assisted genetic algorithm to simultaneously optimize the impeller and volute geometries of a typical centrifugal blood pump, and found that the blade inlet and outlet angles had a significant effect on the pump efficiency and hemolysis index. The Eulerian scalar transport methods¹² used for hemolysis prediction showed high correlation coefficients with experiments, which helps rank different shearing devices.

For the hydrodynamic simulation of oxygenators, Zhang *et al.* studied the flow characteristics of a microporous hollow fiber bundle for the hydrodynamic simulation of oxygenators using CFD.¹³ They concluded that the CFD simulation is a promising approach for the development and optimization of blood oxygenation devices and developed a “two-region” model to more accurately predict oxygen partial pressure distributions.¹⁴ Kaesler *et al.* established a micro-scale CFD model to simulate the oxygen transfer at the fiber level¹⁵ and obtained promising results by including the reaction of oxygen and hemoglobin to oxyhemoglobin directly in the convection–diffusion equation as a source term. Madhani *et al.* targeted 180 ml/min oxygenation and determined the form factor for a hollow fiber membrane (HFM) bundle for oxygenating devices using CFD.¹⁶

For the study of the whole pump-lung system, Taskin *et al.* conducted CFD simulations of wearable artificial pump-lungs with different shapes. They presented and discussed the hydrodynamic and hemolytic performances of different prototypes, including pressure heads and hemolysis indexes.^{4,17} They carried out *in vitro* experiments to verify CFD predictions, which suggest that one can use CFD-based modeling to effectively predict the hydrodynamic and hemolytic performances in such devices.^{18,19} Animal studies were also conducted in sheep to assess *in vivo* hemodynamics, gas-exchange function, and biocompatibility of one device designed using CFD.²⁰ Madhani *et al.* designed a type of artificial pump-lung^{21,22} with form factors determined using CFD (mentioned above), as well as a prototype with circulating blood flow.²³ For the former, they tested the whole system through *in vitro* and *in vivo* experiments. Hours and days of sheep studies tell that the Pittsburgh Ambulatory Assist Lung meets *in vivo* performance targets. For the latter, they analyzed their hydrodynamic properties and shear stress using CFD. In a recent study, Han *et al.* provide an in-depth examination of the development of a pump-lung unit system, with a focus on the progression from a laboratory concept to approval by the Food and Drug Administration for clinical use.²⁴

However, the current state of CFD studies has notable limitations. Existing research primarily focuses on evaluating the hemodynamic performance of the devices and lacks comprehensive analysis of the overall blood flow fields. The hemocompatibility predicted by CFD simulations under various physiologic conditions is often incomplete, and there is a lack of verification of grid convergence and transient patterns in simulation results. These deficiencies in research can lead

to costly prototypes being used in the design and optimization process without a full understanding of their performance. To our knowledge, there are no published works that have thoroughly studied the algorithms and computational costs involved in such problems.

In this study, we present a high-performance computational framework for simulating the blood flow in the artificial pump-lung and the performance of the framework was thoroughly evaluated, taking into account the grid convergence and parallel performance. The framework was then applied to design and evaluate a new artificial pump-lung device, referred to as APL-I (artificial pump-lung-I), which features a magnetically driven centrifugal pump and innovative hollow fiber membranes, resulting in an ultra-compact and assembly free system. We compared the hydrodynamic and biological responses obtained from our simulations with those of previous studies and presented high-resolution flow patterns, including velocity, pressure, and wall shear stress distributions. In addition, we evaluated the parallel performance of our parallel solver by conducting experiments with two different problem sizes to demonstrate its robustness and scalability. Overall, our study provides valuable insights into the hemodynamic performance of wearable artificial pump-lung devices and has significant implications for future studies in this field.

II. METHODS

In this section, we first introduce the concept of the wearable artificial pump-lung (APL) and each component of the device. Second, we show the detailed geometry parameters of the device used in this study, and then, the specific methods and processes of the hemodynamic simulations are given.

A. Concept of the wearable artificial pump-lung

The APL used in this study is a device that combines a magnetically levitated pump/rotor with a uniquely configured hollow fiber membrane (HFM) to provide ambulatory respiratory support for patients with acute or chronic lung diseases.¹⁷ The external outline and internal structure of the APL that we designed (hereinafter referred to as APL-I) are shown in Figs. 1(a) and 1(b), respectively. APL-I comprises an inlet channel, an outlet channel, a membrane, and a maglev centrifugal blood pump. The APL-I is a key component of ECMO that provides respiratory support to patients with acute or chronic lung diseases. It has a prime volume of approximately 300 ml and utilizes a magnetically levitated pump to circulate blood through a uniquely configured hollow fiber membrane. Blood enters the APL-I through an inlet cannula, flows upward through the fiber bundle, and exchanges gas with the sweep oxygen in the membrane holes. The oxygenated blood then exits the APL-I from the blood outlet. As a wearable device, the APL-I and its controller allow patients to be ambulatory. This process is shown in Fig. 2(a), and the wearable nature of the device is illustrated in Fig. 2(b).

We designed the magnetically centrifugal impeller based on the Revolution blood pump (LivaNova PLC, London, UK), as shown in Figs. 2(c) and 2(d), respectively. The Revolution blood pump has an advantage of a low prime volume with a low index of hemolysis.²⁵ To adapt the whole model, motivated by the study of Zhang *et al.*¹⁹ and Han *et al.*,²⁶ our new design adds a central open hole that accommodates the secondary flow path. The fiber material of the fiber bundles is Celgard x30–240 (3M Medical Membranes, Wuppertal, Germany), which is one of the most widely used microporous polypropylene

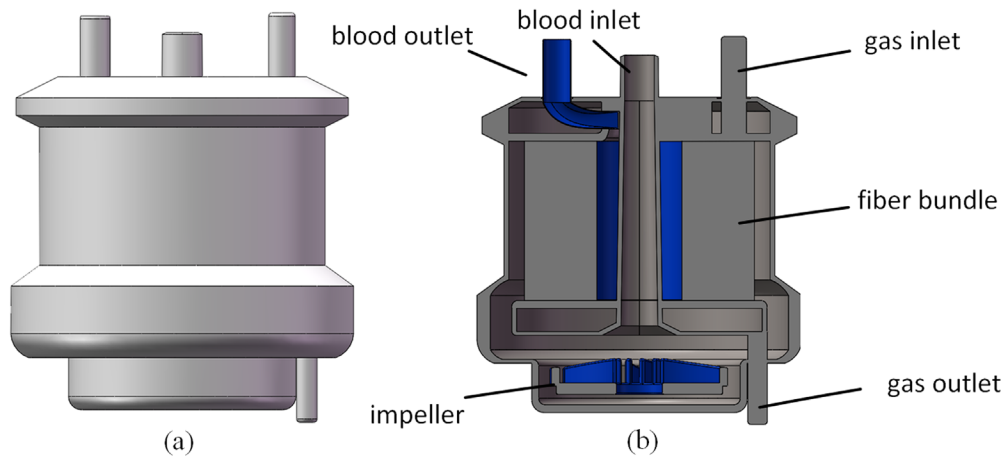


FIG. 1. Geometric characteristics of APL. (a) Front view and (b) internal view.

materials for commercial oxygenators. Celgard x30–240 has an outer diameter of $300\ \mu\text{m}$ and an inner diameter of $240\ \mu\text{m}$, and the total surface area of the fiber tube is $1.05\ \text{m}^2$. Table I shows the detailed parameters of the whole model. The 3D models of APL-I were generated by using a 3D computer-aided design software (Solidworks,

version 2018, Dassault Systemes, Waltham, Massachusetts) based on the parameters listed in Table I.

B. Computational fluid dynamics

As shown in Fig. 3, the computational domain Ω of the hemodynamic simulation in APL-I consists of the free flow domain Ω_f (including the inlet channel, outlet channel, and blood pump area) and the porous medium region Ω_p , that is, $\Omega = \Omega_f \cup \Omega_p$. In this study, the blood flow in the free flow domain is modeled as an incompressible Newtonian fluid with a constant viscosity of $3.5\ \text{mPa}\cdot\text{s}$ and density of $1060\ \text{kg}/\text{m}^3$, as the shear rate in a typical rotary blood pump is relatively high ($>100/\text{S}$) (Refs. 27–29). The transient Navier–Stokes equations are used to model the free flow in APL-I

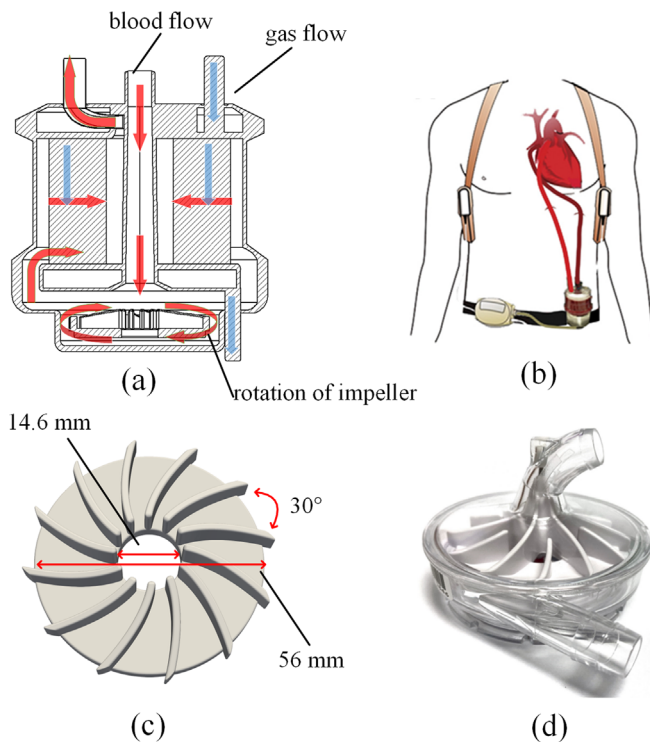


FIG. 2. Conceptualization and usage of APL-I: (a) Conceptualization of the flow path and components for the APL. Here, the red and blue arrows show the path of the blood and gas, respectively; (b) schematic of the patient implanted with APL; (c) the magnetically centrifugal impeller using in APL-I; and (d) the figure of the revolution blood pump referred in this study.

TABLE I. Specification of the APL-I.

Device name	APL-I
Recommended blood flow rate	3–8 L/min
Diameter of the arterial outlet port	9.525 mm
Diameter of the venous inlet port	9.525 mm
Diameter of the gas inlet port	6.35 mm
Diameter of the gas outlet port	5.25 mm
Fiber bundle thickness	22.225 mm
Inner diameter of the fiber bundle	27 mm
Outer diameter of the fiber bundle	73 mm
Porosity (void ratio) of the fiber bundle	0.45
Diameter of the hollow fiber	$300\ \mu\text{m}$
Effective fiber length	50.8 mm
Device length	158 mm
Outer diameter of the blood pump	56 mm
Inner diameter of the blood pump	14.6 mm
Number of blades	12
Discharge angle of the blades	44.5°

28 August 2023 03:21:45

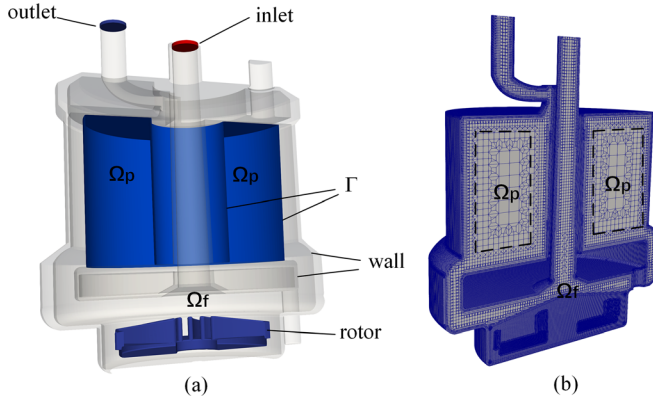


FIG. 3. (a) Computational domain and the boundary setup of the APL-I simulation. (b) An example of the computational mesh.

$$\rho \left(\frac{\partial \vec{v}}{\partial t} + (\vec{v} \cdot \nabla) \vec{v} \right) = \nabla \cdot \bar{\tau} \quad \text{in } \Omega_f, \quad (1)$$

$$\nabla \cdot \vec{v} = 0 \quad \text{in } \Omega_f,$$

where ρ is the density of the blood, $\vec{v} = (v_1, v_2, v_3)$ is the velocity vector of the blood flow, and $v_1, v_2,$ and v_3 are the three components of the velocity. $\bar{\tau} = -p\mathbf{I} + 2\mu\epsilon(\vec{v})$ is the viscous stress tensor, and $\epsilon(\vec{v}) = \frac{1}{2}(\nabla\vec{v} + \nabla\vec{v}^T)$ is the rate-of-strain tensor. Because of the rotor in the pump, the blood flow is turbulent. To capture the turbulence, a turbulence model is needed in the simulation. The $k - \omega$ shear stress transport (SST) turbulence model,¹² which has been shown to be efficient for pump simulations,^{30,31} is employed in this study. The $k - \omega$ SST model is a two-equation eddy-viscosity model, which has the following governing equations:^{32,33}

$$\rho \frac{\partial \omega}{\partial t} + \rho(\vec{v} \cdot \nabla)\omega = -\rho\beta\omega^2 + \nabla \cdot [(\mu + \sigma_\omega\mu_t)\nabla\omega] + \gamma\rho \left\{ [(\nabla \otimes \vec{v}) + (\nabla \otimes \vec{v})^T] : (\nabla \otimes \vec{v}) \right\} + 2\rho(1 - F_1)\sigma_{\omega 2} \frac{1}{\omega} \nabla k \cdot \nabla \omega, \quad (2)$$

$$\rho \frac{\partial k}{\partial t} + \rho(\vec{v} \cdot \nabla)k = \nabla \cdot [(\mu + \sigma_k\mu_t)\nabla k] + \tilde{P}_k - \rho\beta^*\omega k,$$

where k is the turbulence kinetic energy, ω is the specific rate of dissipation, \tilde{P}_k is the effective rate of production of k , σ_k and σ_ω are the diffusion coefficients of the model, and $\sigma_{\omega 1}, \sigma_{\omega 2}, \gamma_1, \gamma_2, \beta_1, \beta_2,$ and β^* are the turbulence modeling constants. β and γ are functions of Menter's blending function, given by

$$\beta = \beta_1 F_1 + \beta_2 (1 - F_1), \quad (3)$$

$$\gamma = \gamma_1 F_1 + \gamma_2 (1 - F_1).$$

γ_1 and γ_2 are given by

$$\gamma_1 = \beta_1 / \beta^* - \sigma_{\omega 1} \kappa^2 / \sqrt{(\beta^*)}, \quad (4)$$

$$\gamma_2 = \beta_2 / \beta^* - \sigma_{\omega 2} \kappa^2 / \sqrt{(\beta^*)},$$

where κ is the von Kármán constant. σ_k and σ_ω are also functions of Menter's blending function, given by

$$\sigma_k = \sigma_{k1} F_1 + \sigma_{k2} (1 - F_1), \quad (5)$$

$$\sigma_\omega = \sigma_{\omega 1} F_1 + \sigma_{\omega 2} (1 - F_1).$$

The Menter's first blending function F_1 is defined as

$$F_1 = \tanh \left\{ \left\{ \min \left[\max \left(\frac{\sqrt{k}}{\beta^* \omega y}, \frac{500 \nu_t}{y^2 \omega} \right), \frac{4\rho\sigma_{\omega 2} k}{CD_{k\omega} y^2} \right] \right\}^4 \right\}, \quad (6)$$

where ν_t is the kinematic viscosity, and the positive portion of cross-diffusion term $CD_{k\omega}$ is defined as follows:

$$CD_{k\omega} = \max \left\{ 2\rho\sigma_{\omega 2} \frac{1}{\omega} \nabla k \nabla \omega, 10^{-10} \right\}. \quad (7)$$

Here, y is the distance to the nearest wall. The operators " \otimes " and " \cdot " refer to the dyadic product and double-dot product (equal to the Frobenius inner product), respectively. μ_t is the scalar dynamic eddy viscosity coefficient defined as

$$\mu_t = \rho\nu_t = \rho \frac{a_1 k}{\max(a_1 \omega, |\Omega| F_2)}, \quad (8)$$

where a_1 is the modeling constant and F_2 is the Menter's second blending function with form

$$F_2 = \tanh \left(\max \left(\frac{2\sqrt{k}}{\beta^* \omega y}, \frac{500 \nu_t}{\omega y^2} \right)^2 \right) \quad (9)$$

and $|\Omega|$ is the absolute value of the mean vorticity vector defined as

$$|\Omega| = \sqrt{\left(\frac{\partial v_3}{\partial x_2} - \frac{\partial v_2}{\partial x_3} \right)^2 + \left(\frac{\partial v_1}{\partial x_3} - \frac{\partial v_3}{\partial x_1} \right)^2 + \left(\frac{\partial v_2}{\partial x_1} - \frac{\partial v_1}{\partial x_2} \right)^2}.$$

The coefficients appearing in Eqs. (2)–(9) are shown in Table II.

1. Porous medium model

The fiber bundle in the APL-I can be considered as a porous medium, and the blood flow in it can be modeled using Darcy's law.^{13,23} According to Darcy's law,^{34,35} the flow velocity in the porous medium \vec{v}_p is directly proportional to the pressure gradient ∇p_p and inversely proportional to the viscosity of the fluid μ . A permeability constant K is used to characterize a particular porous medium^{36,37}

$$\vec{v}_p = -\frac{K}{\mu} \nabla p_p \quad \text{in } \Omega_p. \quad (10)$$

Darcy's law is reliable when the Reynolds number $Re_p = \frac{\rho U \delta}{\mu}$ is less than 1, where δ is the characteristic pore size.³⁸ Otherwise, it is necessary to consider a more general model, such as the nonlinear Forchheimer equation^{38,39}

TABLE II. Value of the coefficients in the $k - \omega$ SST model.

σ_{k1}	σ_{k2}	$\sigma_{\omega 1}$	$\sigma_{\omega 2}$	β_1	β_2	β^*	γ_1	γ_2	κ	a_1
0.85	1.0	0.5	0.856	0.075	0.0828	0.09	5/9	0.44	0.41	0.31

$$\nabla p_p = -\frac{\mu}{K} \vec{v}_p - \frac{\rho C_F}{\sqrt{K}} |\vec{v}_p| \vec{v}_p \quad \text{in } \Omega_p, \quad (11)$$

where C_F is the inertial resistance coefficient. To represent the filtration of the free fluid through Ω_p , suitable coupling conditions are needed on the common interface Γ of the free flow domain Ω_f and porous medium domain Ω_p , that is, (1) continuity of the normal component of the velocity; (2) continuity of the normal stresses across Γ ; (3) the difference between the slip velocity and tangential seepage velocity at the interface is proportional to the shear rate.

In this study, we used a penalization approach to model the flow in the porous media of the APL-I, as the direct coupling of Darcy/Forchheimer equations with the Navier–Stokes equations would have made the solution quite complex because of the intrinsic difference in nature between the equations in the subdomains Ω_f and Ω_p . The penalization method involves modifying the Navier–Stokes equations by incorporating two penalization terms that account for the resistance created by the porous medium, and these terms are based on the linear Darcy and nonlinear Forchheimer equations⁴⁰

$$\begin{aligned} \rho \left(\frac{\partial \vec{v}}{\partial t} + (\vec{v} \cdot \nabla) \vec{v} \right) &= \nabla \cdot \bar{\tau} + P_v \vec{v} + P_i |\vec{v}| \vec{v} \quad \text{in } \Omega_p, \\ \nabla \cdot \vec{v} &= 0 \quad \text{in } \Omega_p, \end{aligned} \quad (12)$$

where $P_v = \frac{\mu}{K}$ and $P_i = \frac{\rho C_F}{\sqrt{K}}$.

The penalized model for the porous medium is much easier to couple the Navier–Stokes equations for the free flow, since they have similar formulations and do not need any special interface conditions on the common interface.

The whole model for the blood flow simulation in the pump-lung can be written in the following form:

$$\begin{aligned} \rho \left(\frac{\partial \vec{v}}{\partial t} + (\vec{v} \cdot \nabla) \vec{v} \right) &= \nabla \cdot \bar{\tau} + P_v \vec{v} + P_i |\vec{v}| \vec{v} \quad \text{in } \Omega, \\ \nabla \cdot \vec{v} &= 0 \quad \text{in } \Omega, \\ \rho \frac{\partial \omega}{\partial t} + \rho (\vec{v} \cdot \nabla) \omega &= \nabla \cdot [(\mu + \sigma_\omega \mu_t) \nabla \omega] \\ &+ \gamma \rho \left\{ [(\nabla \otimes \vec{v}) + (\nabla \otimes \vec{v})^T] : (\nabla \otimes \vec{v}) \right\} \\ &- \rho \beta \omega^2 + 2\rho(1 - F_1) \sigma_{\omega 2} \frac{1}{\omega} \nabla k \cdot \nabla \omega \quad \text{in } \Omega, \\ \rho \frac{\partial k}{\partial t} + \rho (\vec{v} \cdot \nabla) k &= \nabla \cdot [(\mu + \sigma_k \mu_t) \nabla k] \\ &+ \tilde{P}_k - \rho \beta^* \omega k \quad \text{in } \Omega, \end{aligned}$$

with some boundary conditions defined in Table III, where

TABLE III. Boundary conditions of variables applied in this study.

Boundary	Velocity \vec{v}	Pressure p	k	ω
Inlet	Fixed value	Zero-gradient	Fixed value	Fixed value
Outlet	Zero-gradient	Fixed value	Inlet–outlet	Inlet–outlet
Wall	No-slip	Zero-gradient	kqR wall function	Omega wall function
Rotor	Moving wall velocity	Zero-gradient	kqR wall function	Omega wall function

$$P_v = \begin{cases} 0 & \text{in } \Omega_f, \\ \frac{\mu}{K} & \text{in } \Omega_p, \end{cases} \quad \text{and} \quad P_i = \begin{cases} 0 & \text{in } \Omega_f, \\ \frac{\rho C_F}{\sqrt{K}} & \text{in } \Omega_p. \end{cases}$$

Indeed, most commercial packages, which are capable of simulating flows in domains partially occupied by porous medium, are based on this approach, whose results are not dramatically different from coupled models from the macroscopic viewpoint.³⁸ According to Darcy’s law, the permeability K of the porous medium can be calculated as

$$K = \frac{d_0^2}{150} \frac{\xi^2}{(1 - \xi)^2}, \quad (13)$$

where d_0 is the diameter of the hollow fibers and ξ is the porosity of the fiber bundles, whose values are listed in Table I. In Eq. (12), when the flow Q is less than 6.0 L/min, the last term $P_i |\vec{v}| \vec{v}$ can be ignored.⁴¹

2. Hemolysis index calculation

For the prediction of the hemolysis of the pump-lung, a numerical method called fast three-dimensional numerical hemolysis approximation, introduced by Garon and Farinas,⁴² is used to calculate the Normalized Index of Hemolysis (NIH) defined in the American Society for Testing and Materials (ASTM) standard. This method directly calculates the hemolysis index from the velocity and shear stress fields, thus avoiding the problems caused by the previous calculation of blood damage along several particle paths. The damaged fraction of erythrocytes $D(t, \tau)$ within the blood volume of the experimental setup is defined as the ratio of the plasma-free hemoglobin (fHb) to the total hemoglobin within the blood volume (Hb). The damaged fraction $D(t, \tau)$ is assumed to be a polynomial function of the shear stress τ and exposure time t according to papers^{42,43}

$$D(t, \tau) = \frac{\text{fHb}}{\text{Hb}} = C \tau^a t^b. \quad (14)$$

To avoid the nonlinearity of the exposure time t in Eq. (14), a linear damage index D_I is introduced, which is defined as

$$D_I = D(t, \tau)^{\frac{1}{a}} = C^{\frac{1}{a}} \tau^{\frac{b}{a}} t. \quad (15)$$

Garon and Farinas⁴² have developed a fast three-dimensional numerical hemolysis approximation method based on the hyperbolic transport equation to calculate the linear damage index

$$\left(\frac{\partial}{\partial t} + \vec{v} \cdot \nabla \right) D_I = \sigma, \quad (16)$$

where \vec{v} is the velocity obtained in the CFD simulation and the source term σ is the hemolytic destruction rate per unit time

$$\sigma = C^{\frac{1}{a}} \tau^{\frac{b}{a}}, \tag{17}$$

and we use a set of parameters proposed by Zhang *et al.*:⁴⁴ $C = 1.228 \times 10^{-7}$, $a = 0.6606$, and $b = 1.9918$, which deliver one of the best agreements with experimental values.⁴⁵ The shear stress τ is calculated based on the von Mises yield criterion^{11,46}

$$\tau = \sqrt{\frac{1}{6} \sum (\tau_{ii} - \tau_{jj})^2 + \sum \tau_{ij}^2}, \tag{18}$$

where $\tau_{ij} = -p\delta_{ij} + \mu \left(\frac{\partial v_i}{\partial x_j} + \frac{\partial v_j}{\partial x_i} \right)$ is the principal stress and δ_{ij} is the Kronecker delta. As suggested in Ref. 42, when the flow in APL-I reached a steady state after some iterations, the average linear damage \bar{D}_I can be used to calculate the hemolysis index, which is calculated by integrating both sides of Eq. (16) over the domain Ω ,

$$\bar{D}_I = \frac{1}{Q} \int_{\Omega} \sigma dV, \tag{19}$$

where Q is the volume flow obtained by integrating the velocity \vec{v} over the computational domain Ω . Then, the damaged fraction is computed by $D(t, \tau) = (\bar{D}_I)^a$, and the hemolysis index NIH is evaluated by

$$\text{NIH} = \text{Hb} \times D(t, \tau) \times 100, \tag{20}$$

where Hb is the hemoglobin concentration and is assumed to be 140 g/L for the human blood.

3. Mesh generation

The meshes used in this simulation are generated by the OpenFOAM self-contained mesh generator snappyHexMesh, which is a fully parallel and split hex mesh generator that guarantees a maximum mesh quality. To better resolve the detail of the flow structure, the nonuniform meshes are used; that is, the mesh in the area that has complicated flows is relatively fine, and the other area is relatively coarse. An example of the three meshes used in this simulation is shown in Fig. 4, where the mesh sizes are about 0.38, 0.33, and 0.24 mm, respectively.

4. Simulation algorithms

The simulation in this study is carried out using the open-source computational fluid dynamics (CFD) tool OpenFOAM, which is known for its accessibility, transparency, customization, and extensibility. To compare with previous studies, multiple flow rates and rotational speeds are analyzed, as shown in Table IV. The sliding mesh boundary method, which is supported by OpenFOAM's Arbitrary

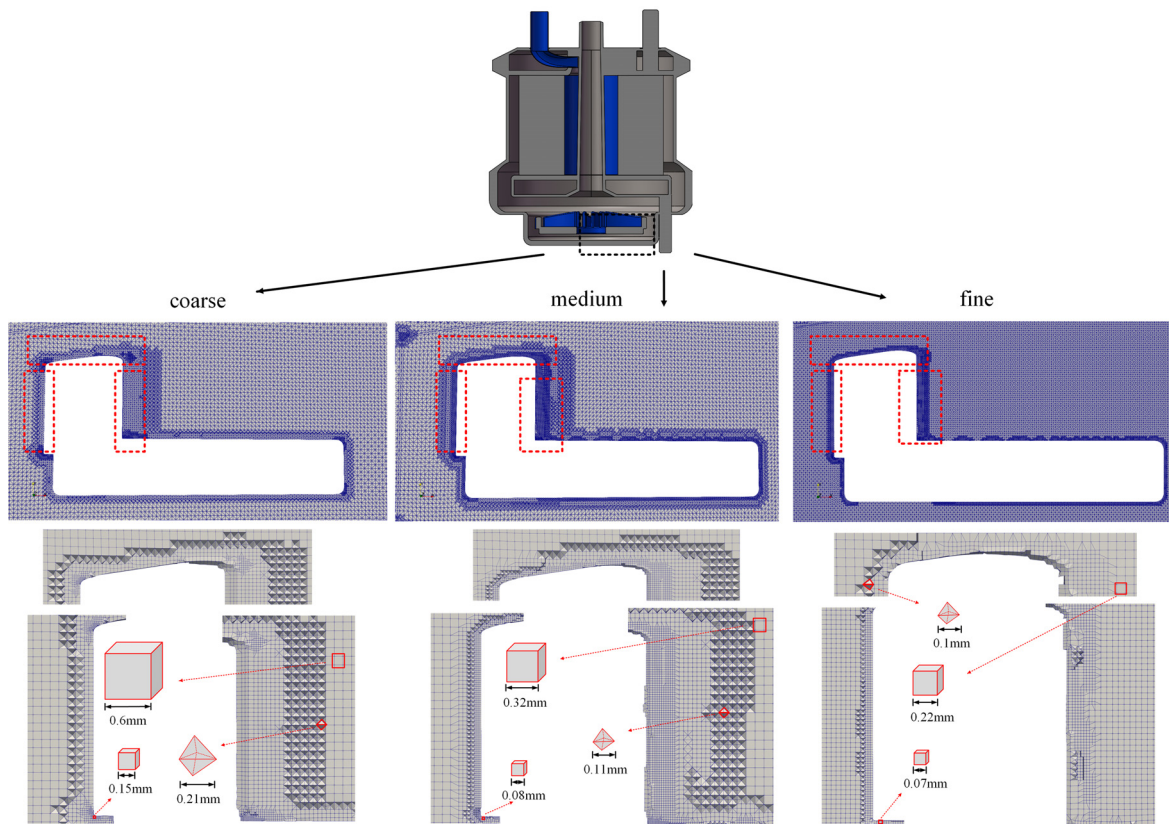


FIG. 4. A detailed cross-sectional view of the three computational meshes around the impeller blade tip.

TABLE IV. Eight test physiologic conditions used to evaluate APL-I in this study.

Condition #	Flow rate (L/min)	Rotational speed
1.1/1.2/1.3/1.4	3/4/5/6	3000
2.1/2.2/2.3/2.4	3/4/5/6	1500

Mesh Interface (AMI) library, is used to handle the rotation of the impeller. This method uses interpolation to account for the motion of adjacent cell faces at each time step.¹⁰

For the transient simulation of blood flows, this study employs a segregated algorithm named PIMPLE, which decouples the velocity and pressure and solves them iteratively. The PIMPLE algorithm combines the Pressure Implicit with Splitting the Operators (PISO) and Semi-Implicit Method for Pressure-Linked Equation (SIMPLE) algorithms. At each time step, the momentum equation is solved by using the pressure and velocity fields of the previous time step. Then, PISO loop is entered, and the Poisson equation is solved several times using the geometric algebraic multi-grid (GAMG) method.⁴⁷ The velocity and flux are then corrected, and the solver moves on to the next SIMPLE iteration. The PIMPLE algorithm enables the under-relaxation of variables during each iteration of the SIMPLE method. This provides enhanced numerical stability and the ability to adopt larger Courant numbers; that is, we can use larger time steps in the simulation.⁴⁸ The flowchart of the PIMPLE algorithm is shown in Fig. 5. A detailed explanation of the PISO and SIMPLE algorithms can be found in Ref. 49. A second-order upwind scheme is selected for the

solutions of the momentum, turbulence, and scalar transport equations to keep the accuracy of calculations. The residual value (convergence criteria) is set to 10^{-6} for all solutions of equations considered at every time step. After a few rotations of the blood pump, the simulations were considered convergent based on the following criteria: (1) all monitored residuals were smaller than 10^{-6} , (2) the outlet pressure reached a steady level, and (3) the relative difference in the flow rate between the inlet and outlet was less than 5%. Eight different physiologic conditions listed in Table IV are used to analyze the performance of APL-I. All the numerical experiments are run on the ORISE super-computer at the Chinese Academy of Sciences, which has a 32-core Hygon C86-7185 2.5 GHz CPU and 128 GB RAM per computing node. The operating system of the cluster is Red Hat 4.8.5-36, and the simulation is based on the newest OpenFOAM-v2012.

5. Mesh convergence study

The accuracy and efficiency of the simulation are strongly related to the computational mesh, and the mesh convergence study is always the first step to verify the numerical simulation algorithm. Here, we created three meshes for the mesh convergence study, which has 8.49×10^6 (coarse), 12.42×10^6 (medium), and 19.64×10^6 (fine) polyhedral cells, respectively. Condition 1.3 (5 L/min, 3000 RPM) and the simulated flow rate at the outlet and the pressure head are used for the mesh convergence study.

From Figs. 6(a) and 6(b), we see that the difference between the “medium” and “coarse” meshes is about 2% for the flow rate and 1% for the pressure head, and the difference between the “fine” and “medium” meshes is even smaller, which is 0.7% for the flow rate and 0.013% for the pressure head, respectively. Here, we further study the mesh convergence using the Grid Convergence Index (GCI) introduced by Roache.⁵⁰ GCI demonstrates how much the computed value is different from the asymptotic value, as well as how much the solution of the computed value would change with further mesh refinement.⁵¹ The definition of GCI is

$$GCI_{i+1,i} = F_s \frac{|e_{i+1,i}|}{f_i(r^m - 1)}, \tag{21}$$

where F_s is the safety factor, which is 1.25 as suggested in Wilcox’s book,⁵² f_i is the discrete solution on the i th mesh, $e_{i+1,i} = f_{i+1} - f_i$ is the difference between f_{i+1} and f_i , and $i = 1, 2, 3$ corresponding to the fine, medium, and coarse mesh, respectively, in this paper. r is the ratio of the mesh refinement, that is,

$$r = \frac{\text{The total number of cells of the fine mesh}}{\text{The total number of cells in the medium mesh}}, \\ = \frac{\text{The total number of cells in the medium mesh}}{\text{The total number of cells in the coarse mesh}}, \tag{22}$$

which is about 1.49 in our mesh convergence study. m is the order-of-accuracy, which is defined as

$$m = \frac{\ln\left(\frac{\varepsilon_{3,2}}{\varepsilon_{2,1}}\right)}{\ln(r)}. \tag{23}$$

In this case, for the average flow rate at the outlet and the pressure head (mm Hg), since we have reached the monotonic convergence

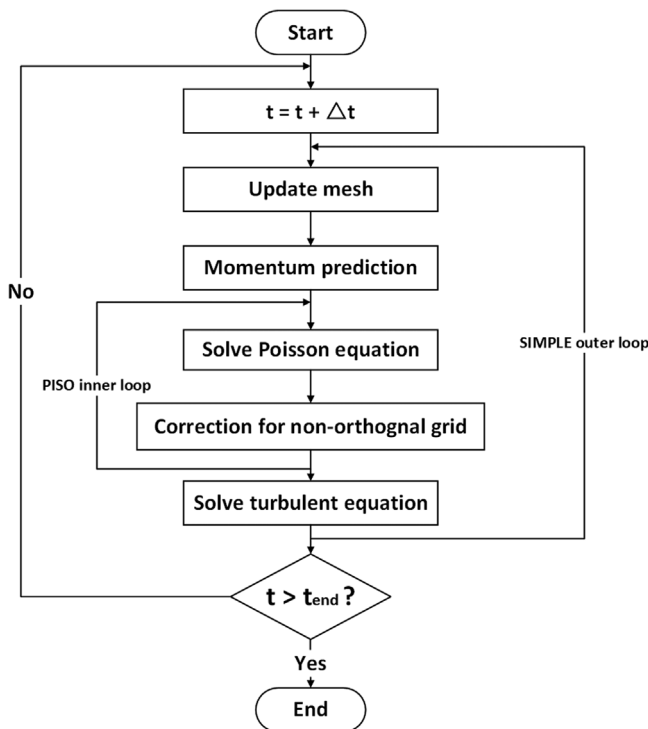


FIG. 5. Flowchart of the PIMPLE algorithm.

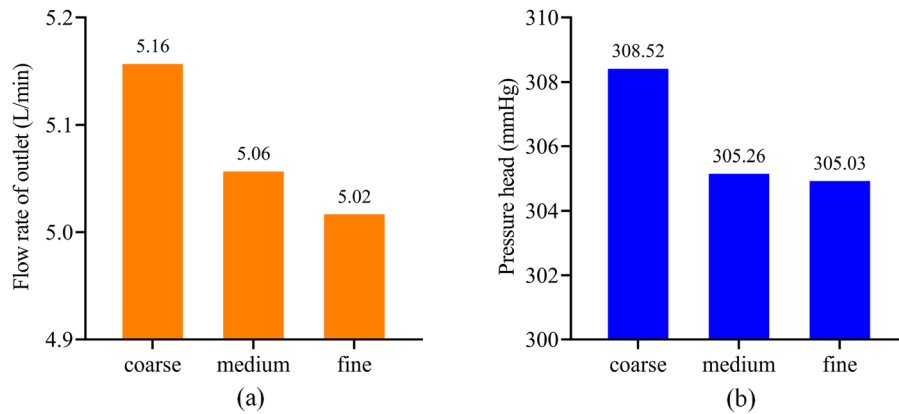


FIG. 6. Results of mesh refinement: (a) Volumetric flow rate and (b) pressure head.

condition of this system ($0 < \frac{\epsilon_{2,1}}{\epsilon_{3,2}} < 1$) (Ref. 51), we can directly obtain the GCI from Eq. (21), which is shown in Table V. The results in Table V show that the differences between medium and fine meshes for the volumetric flow rate and pressure head are very small, which are 0.66% and 0.0075%, respectively.

To further verify the mesh independence and make it more clear, we show the velocity magnitude (m/s) profiles and wall shear stress (WSS) magnitude (Pa) profiles along a line in the xz plane. Since WSS is only defined on the surface of APL-I, while the velocity is zero on the surface since we are using the no-slipping boundary condition on the surface. So, we show the velocity and WSS profiles on two different lines; that is, the y -ordinates for the lines to show velocity and WSS are -0.001 m (in the fluid domain) and -0.003 m (on the surface of the rotor), respectively. From Fig. 7, we find that the max velocity of the medium mesh (9.90 m/s) is closer to the fine mesh (10.53 m/s), compared with the coarse mesh at the same x -ordinate (7.60 m/s). More apparently, in Fig. 7(c), the profile of the coarse mesh is very different from the other two. The possible reason is that the coarse mesh is too coarse to capture the external characteristics of the rotor. The $GCI_{3,2}(\%)$ and $GCI_{2,1}(\%)$ for the max velocity magnitude are 8.8 and 2.88, respectively. Due to the small differences between the medium mesh and fine mesh, the medium (12.42×10^6 cells) mesh will be used for the rest of the simulation.

The time step size Δt is also a crucial parameter in the simulation algorithm. In our simulation, the time step size is determined and controlled by the max Courant number, which is defined as

$$C = \frac{\Delta t}{2V} \max_{\text{all cells}} \sum_{i=1}^m |\phi_i|, \quad (24)$$

TABLE V. Grid convergence index (GCI) and order of accuracy for parameters volumetric flow rate and pressure head.

	$\epsilon_{3,2}$	$\epsilon_{2,1}$	$GCI_{3,2}(\%)$	$GCI_{2,1}(\%)$
Volumetric flow rate	0.1	0.04	1.64	0.66
Pressure head	3.26	0.23	0.1	0.0075

where V is the cell volume, ϕ_i is the volumetric flux on the i th face, and m is the number of faces of a cell.⁴⁸ The time step size is automatically adjusted at each time step based on the maximum Courant number, since the flux in Eq. (24) varies from step to step, which causes the time step size to vary accordingly. To assess the temporal stability of the simulation, we tested three different values of the maximum Courant number (C), which were set to 1.0, 2.0, and 3.0, respectively. The velocity magnitude profiles along the x axis at the outlet patch, as obtained with different values of C , are shown in Fig. 8. The results show that the maximum difference in the velocity magnitude between the conditions $C=1.0$ and $C=3.0$ was only 0.13%. To minimize the simulation time, we used a maximum Courant number of 3.0 for the remainder of this study. The total simulation time is approximately 10 h, when 120 CPU cores are utilized.

III. SIMULATION RESULTS AND DISCUSSION

In this section, we show the details of the simulation results, including the distribution of the velocity, pressure, wall shear stress, and biological response, as well as the parallel performance of the simulation algorithms. We chose to use the results of condition 1.3 (5 L, 3000 r/min) for visualization and analysis since it satisfies the physiological operating condition (pressure head $>= 120$ mm Hg at 5 L/min) and is easy to compare with similar studies.^{13,19} We also compare our simulated results (pressure head) with published studies.

A. Hemodynamic analysis of APL-I

Figure 9 shows the velocity distribution with condition 1.3 (5 L, 3000 r/min) on different cross sections: (a) the central vertical cross section of APL-I, (b) the central vertical cross section of the porous region, and (c) the horizontal cross section through the impeller. As expected, the blood flow goes into APL-I at a constant speed at the inlet, and it goes through the inlet channel and is accelerated by the pump. The peak velocity appears at the tip region of the blade [see Figs. 9(a) and 9(c)]. Then, the blood flow goes upward along the impeller surface into the porous region, and a small part of the flow enters the center eye of the impeller and goes into the blade passages with a 90° diverting, forming the second flow channel. Some small symmetrical vortexes come up above the blades, as shown in Fig. 9(a).

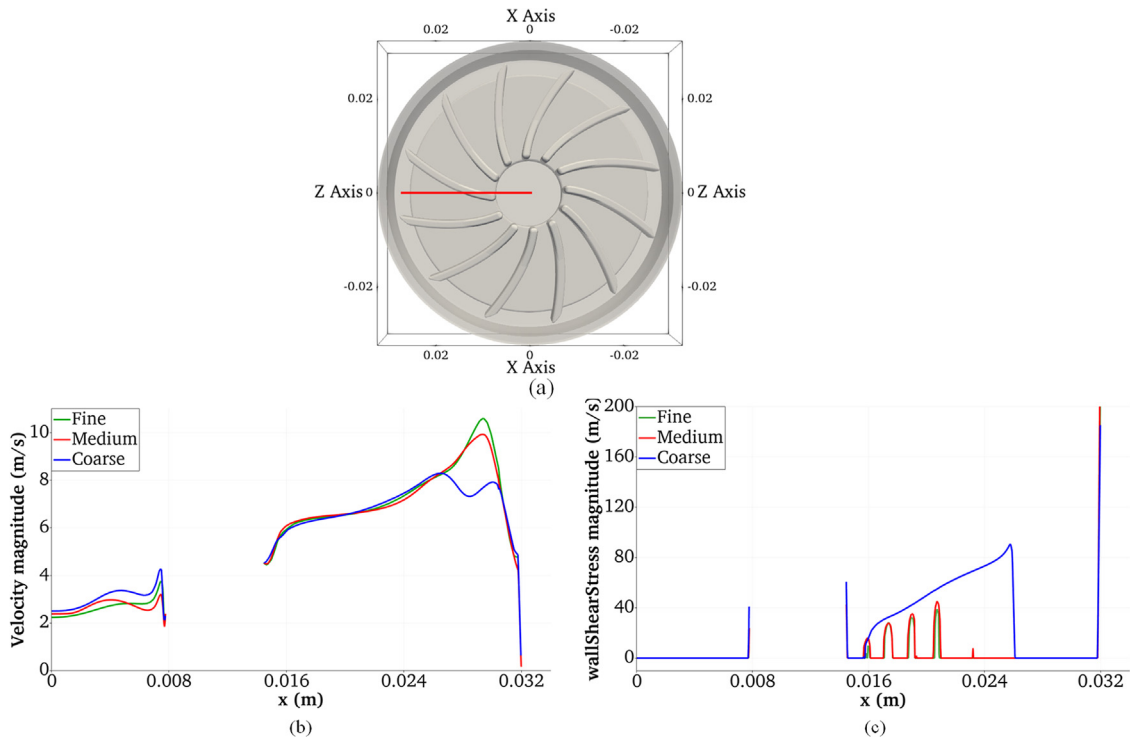


FIG. 7. Mesh convergence study of the velocity magnitude (b) and wall shear stress magnitude (c) along a line on the xz plane (a) at the condition 1.3 (5L/min, 3000 RPM) using three different meshes: “coarse” (blue), “medium” (green), and “fine” (red).

From Fig. 9(b), we see that the blood flow speed is relatively low (less than 0.5 m/s) as it goes through the fiber bundles from outside to inside under the action of the fiber bundle resistance. To better show the velocity distribution, we use different ranges for the color bar in Fig. 9. Furthermore, it is evident that the velocity is layering when the blood flow goes through the fiber bundles. Finally, the blood is collected in the arc-shaped outlet channel and goes out of the pump-lung at the outlet without apparent vortex or reflux. From the velocity distribution, it can be observed that there is a region of low speed in the

bottom center of the pump, which could lead to prolonged residence time for the blood in this area, potentially resulting in the formation of blood clots. Therefore, further optimization of the pump is necessary.

Figure 10 shows the pressure distribution with condition 1.3 on the cross sections defined in Fig. 9. The pressure at the inlet is set to 0 mmHg, which can be viewed as a reference pressure, and it slightly drops from the top to the bottom of the inlet channel. A negative pressure area appears in the pump, which sucks in the blood flow from the inlet and then pushes the flow up toward the fiber bundles. A significant pressure rise is generated with the rotation of the impeller when the blood flows across the blades [see Figs. 10(a) and 10(c)]. The pressure drops about 30 mmHg when it goes through the fiber bundles due to the high viscous resistance in this area [Fig. 10(b)]. With the collection of the blood in the outlet channel, since the area of the outlet boundary is much smaller than the area of the cross section of the outlet channel, the pressure gradually increases and reaches the peak at the outlet.

Figure 11 shows the streamline and vector field of the velocity in APL-I: (a) front view of the central planar cut plane, (b) top view of the central planar cut plane. From Fig. 11(a), we can see that the blood is driven from the impeller in all directions and then scatters in fiber bundles with a layering flow at a low speed. From Fig. 11(b), we can see that the exit flow from the blade passage is relatively well distributed. No localized small vortices or flow disturbances at the impeller eye are noticed, but some large vortices are observed in the channels. The formation of unnatural vortices in the blood flow can impact the momentum transfer and increase energy dissipation. To minimize the

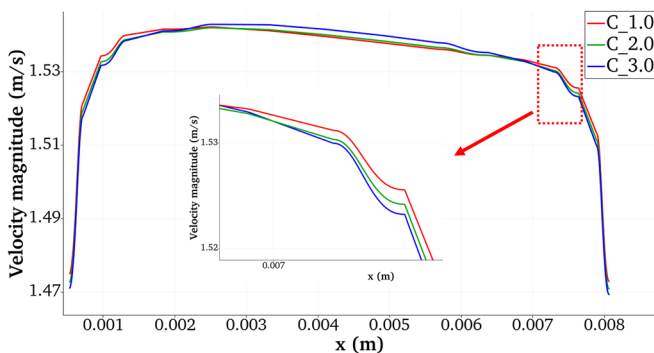


FIG. 8. The time step convergence study of the algorithm in terms of the velocity magnitude along the x axis at the outlet patch using different Courant numbers. Here, C_1.0, C_2.0, and C_3.0 refer to the results obtained with $C = 1.0$, $C = 2.0$, and $C = 3.0$, respectively.

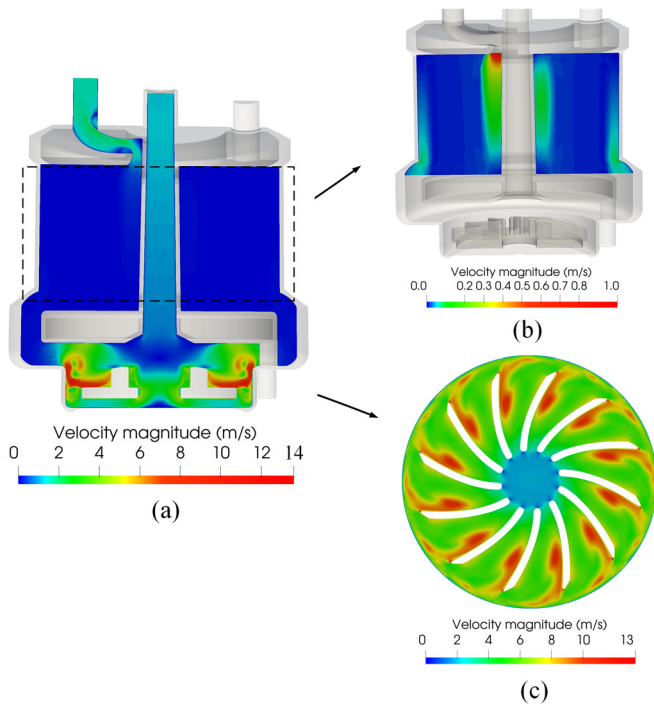


FIG. 9. Velocity magnitude (m/s) distribution of the blood flow in the pump-lung. (a) The central vertical cross section of APL-I; (b) the central vertical cross section of the porous region; (c) the horizontal cross section through the impeller.

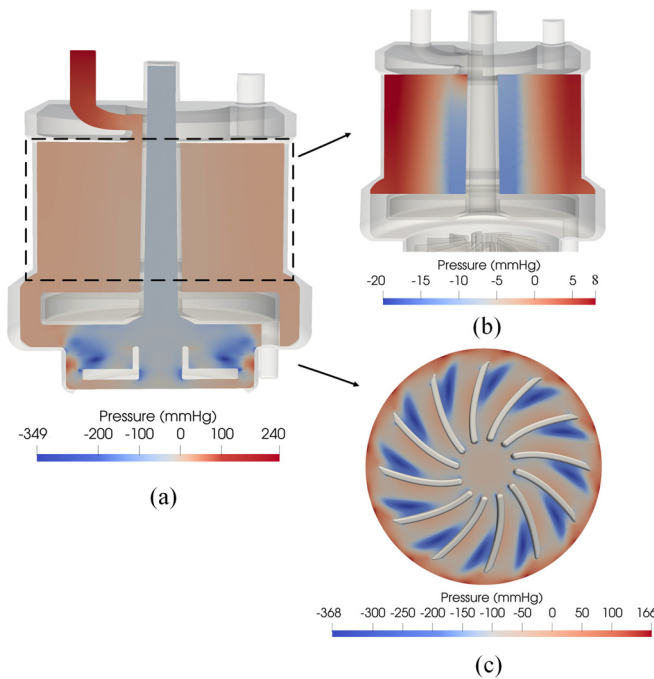


FIG. 10. Pressure (mm Hg) distribution. (a) The central vertical cross section of APL-I; (b) the central vertical cross section of the porous region; (c) the horizontal cross section through the impeller.

adverse effects of these vortices, further optimization is necessary to reduce the vortices generated by the pump.

Figure 12 depicts the hydrodynamic pumping function of the APL-I device as determined through CFD simulations. The generated pressure heads vs flow rate (H-Q curves) under different physiologic conditions are compared with the results of Zhang’s IMPO.¹⁹ From Fig. 12, we see that APL-I has a larger pressure head (> 150 mmHg) compared with IMPO over different physiologic conditions. This is likely due to the better rotor shape, optimized flow channel, and appropriate number of blades of APL-I. The pressure head reaches 425.9 mmHg for the condition 1.1 (3.0 L/min, 3000 RPM). With the increase in the volumetric flow rate at the inlet, the pressure head decreases linearly to 252.02 mmHg for the condition 1.4 (6.0 L/min, 3000 RPM). These values are lower for conditions 2.1–2.4, which have a lower rotation speed (1500 RPM). According to our simulation results, the APL-I device meets the biocompatibility requirement under the targeted physiological operating condition (pressure head of 120 mmHg at 5 L/min) under three different conditions.

Figure 13 shows the distribution of the wall shear stress for the condition 2.3 (1500 RPM, 5.0 L), where the plot only includes wall shear stress values that are higher than 50 Pa. The wall shear stress was calculated by multiplying the shear stress tensor with the normal vector of the surface that faces into the domain, as described in Ref. 53. The plot of the wall shear stress distribution for condition 2.3 (1500 RPM, 5.0 L) shows that there are some high-stress spots on the impeller wall and blade tips, with values of approximately 180 Pa. As shown in Fig. 9, there is a swirling motion near the leading edge of the impeller that could expose the blood to higher shear stress. These high-stress areas need to be addressed in future optimization efforts, as high wall shear stress has been shown to have the potential to cause blood damage. However, the shear stress levels in most of the flow domains do not exceed the threshold for blood damage, which is around 100 Pa (Ref. 19).

Figure 14 displays the predicted NIH values for APL-I, calculated using a fast three-dimensional numerical approximation method based on the simulation results. The results indicate that at a flow rate of 5 L/min and a rotational speed of 1000 RPM, the predicted NIH value is less than 0.001 g/100 L, which meets the biocompatibility requirement of 0.1 g/100 L. As the rotational speed increases, the NIH value increases to 0.008 28 g/100 L at 1500 RPM and 0.0799 at 2000 RPM. This increase is mainly due to the higher shear stress generated by the turbulent flow around the blades. Our results show that APL-I has a good hemolytic performance under the targeted physiological operating condition, and its NIH values are comparable to other published pump oxygenators. In particular, under the same flow condition (5 L/min), its NIH values are significantly lower than previous products (IMPO and PediPL). From the results in Table VI, it is evident that the NIH values for the pump-lung simulations are significantly higher than those for the pump-only simulations. This can be attributed to the presence of fiber bundles in the pump-lung device. The parameters can also have a significant impact on the values of NIH. For example, this set of parameters we use can effectively prevent over predicting of NIHs.⁴⁵ Overall, APL-I has a reasonable pressure head that is allowed by human physiology (5 L/min, 140.07 mm Hg) and comparatively low hemolysis, making it a promising candidate for further development and application.

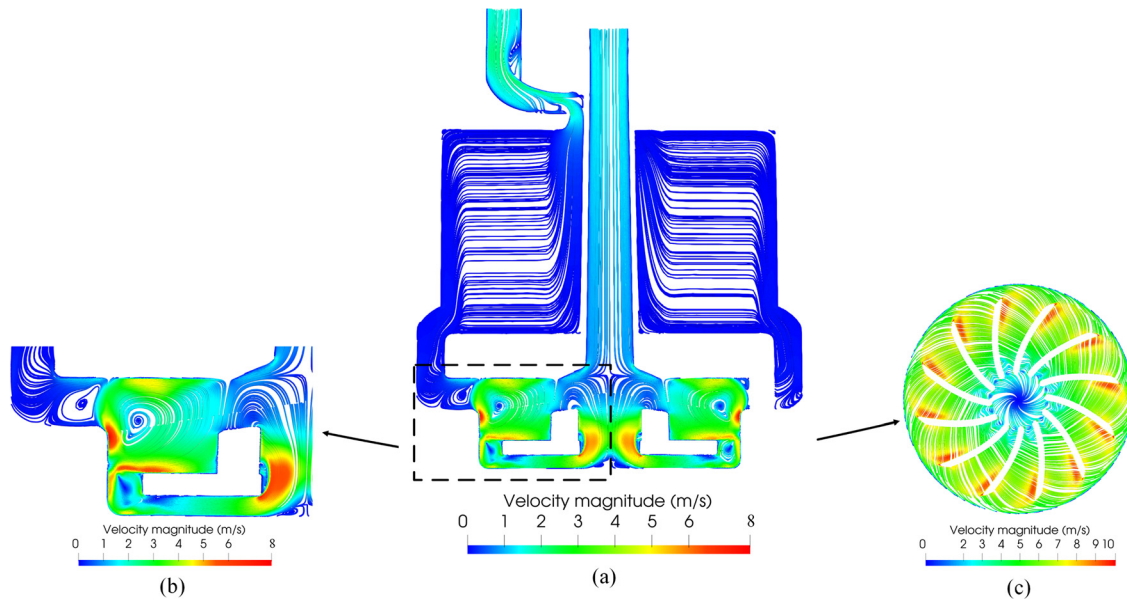


FIG. 11. II-7 The 2D streamline distribution in APL-I: (a) The central vertical cross section of APL-I; (b) a zoom-in view of the area near the impeller; (c) the horizontal cross section through the impeller.

B. Parallel performance of the simulation algorithm

Today’s supercomputer has a large number of processor cores and offers significant computational power. To fully exploit the computing power of the supercomputer for fast and high-resolution CFD simulations, it is crucial that the simulation algorithms possess good parallel scalability and efficiency. In this section, we perform an in-depth analysis of the parallel performance of the simulation algorithm and identify factors that might affect its scalability and efficiency.

Our simulations involve the coupling of two flows with distinct properties (free flow and porous media flow), a moving domain, and relative motions in a single configuration, making the parallelization

process highly nontrivial. To study the parallel performance, we generated two unstructured meshes with varying mesh cells, which have 12.42 and 29.6×10^6 cells, respectively. We used the condition 2.3 (5 L/min blood flow rate and 3000 RPM rotation speed) for our analysis and recorded the runtime for the first 15 time steps. The results of our parallel performance analysis are depicted in Figs. 15(a) and 15(b), respectively.

As we can see from Fig. 15(a), with the increase in the number of processors, the total runtime for both mesh cases decreases quickly. When the number of processors reaches 768, the runtime decreases to 37.62 and 72.48 s, respectively. The speedup for both cases is almost linear when the number of processors is less than 192, as shown in Fig. 15(b), and with increasing the number of processors, the speedup drops. The parallel efficiency and speedup of the large mesh case are better than those of the small mesh case. The parallel efficiencies for the small and large meshes reach 33.5% and 51.6%, respectively, when the number of processors reaches 768. The ratio of the computation cost on each processor and the communication cost among processors, which is higher for the large mesh case compared to the small mesh case, is the main factor that reduces the parallel efficiency.

Table VII shows the parallel performance of the four main parts of the simulation algorithm. From the table, we can see that mesh updating and solution of the Poisson equation take up most of the time, accounting for about 70% of the total time. The momentum prediction and the solution of the turbulence equations have superlinear speedup, meaning that when the number of processors doubles, the computing time reduces more than 50%. However, the parallel efficiency of the mesh updating and the Poisson equation solution is low, especially for the solution of the Poisson equation, which has a parallel efficiency of 43% for the large mesh case.

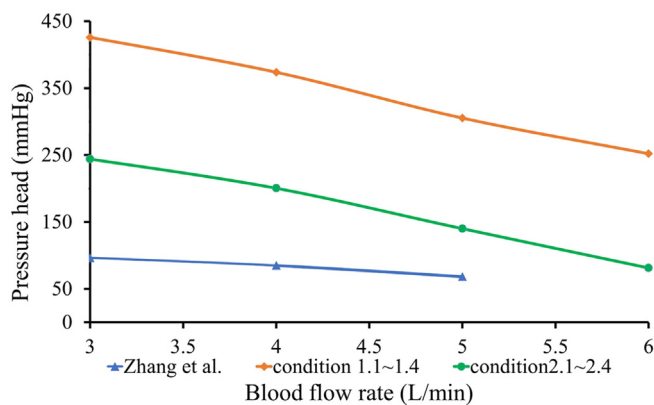


FIG. 12. Hydrodynamic pumping functions of APL-I at different physiologic conditions.

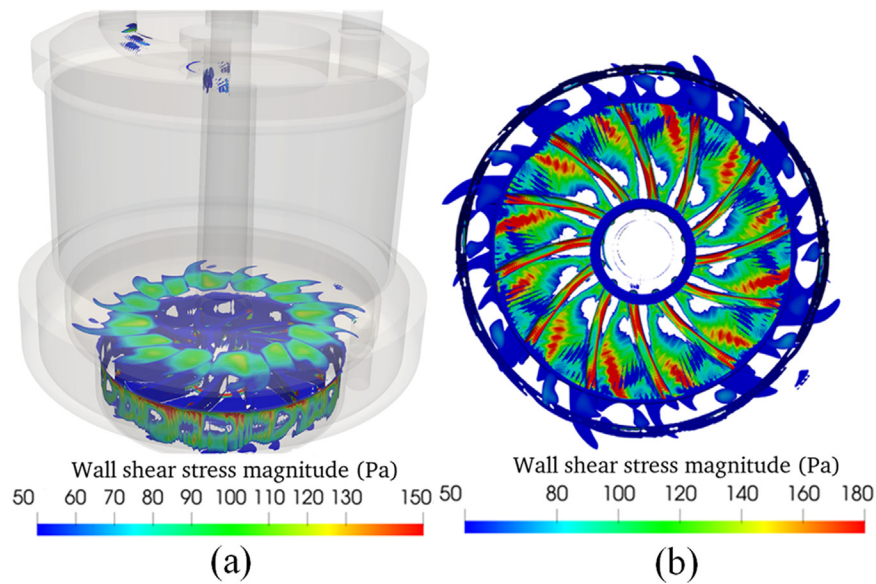


FIG. 13. The high wall shear stress region. (a) Front view and (b) bottom view.

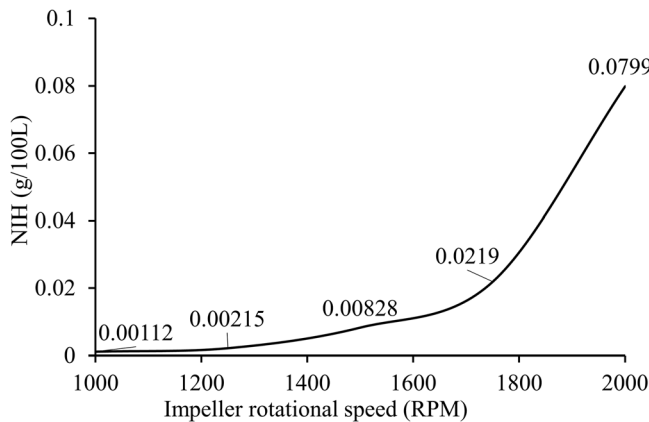


FIG. 14. Predicted hemolysis evaluation of APL-I at different rotational speeds.

In conclusion, based on the parallel performance results, the simulation algorithm is robust and scalable for hundreds of processors. To achieve better scalability and efficiency and allow for use with more processors, further optimization is necessary, especially for the solution of the Poisson equation and mesh updating algorithms.

TABLE VI. Comparison of the hemolytic performance of APL-I with previous pump-oxygenators.

Device	Hemolysis index NIH (g/100 L)	Operating condition	Source
Artificial pump-lung (APL-I)	0.008 28	5.0 L/min, 1500 RPM, 140.07 mmHg	Present work
Levitronix CentriMag blood pump	0.0029	5.0 L/min, 4000 RPM, 350 mmHg	Zhang <i>et al.</i> ⁵⁴
Integrated maglev pump-oxygenator (IMPO)	0.04	5.0 L/min, 3000 RPM, 125 mmHg	Zhang <i>et al.</i> ²⁰
Pediatric pump-lung (PediPL)	0.04	2.5 L/min, 3200 RPM, 100 mmHg	Wu <i>et al.</i> ⁵⁵
FDA benchmark blood pump	0.003 09	6.0 L/min, 2500 RPM, 51.1 mmHg	Good and Manning ¹⁰

IV. CONCLUSION

In conclusion, a comprehensive high-performance pump-lung coupled simulation framework has been introduced and evaluated, which includes a detailed study of the mathematical model, solution algorithms, mesh convergence, and parallel performance. A wearable artificial pump-lung was designed and analyzed using high-resolution CFD simulations with this framework. Hydrodynamic and hemolytic performances of this device are compared with previous studies, which show promising results. High-resolution patterns of the flow field are presented and analyzed. The mesh convergence and parallel performance of the simulation algorithm are also studied in detail.

The simulation results show that the highest blood velocity regions are mainly distributed at the level of rotational blades, which can reach a speed of larger than 13 m/s at a condition of 5 L/min and 3000 RPM. The pressure head is generated with the rotation of the impeller and then drops about 20–30 mm Hg when it goes across the fiber bundles. Regions with higher wall shear stress are mainly distributed at the wall of the impeller, which needs further optimization. According to this simulation, this device meets the target performance requirements in terms of the pressure head and the hemocompatibility under the physiologic conditions mentioned above, but there is still room for improvement.

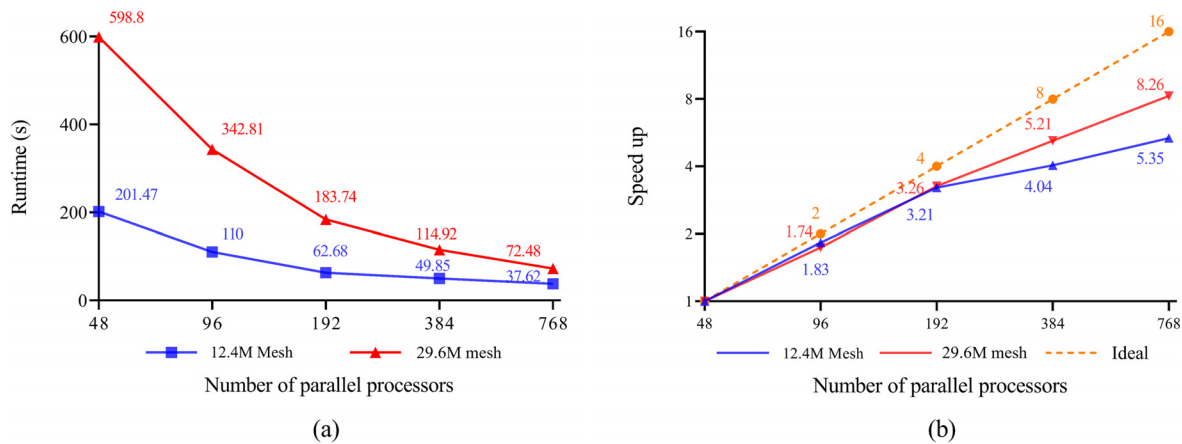


FIG. 15. Parallel performance of the simulation algorithm. (a) The total simulation time of the first 15 time steps; (b) the parallel speedup. 12.4M Mesh and 29.6M Mesh refer the meshes with 12.4 and 29.6×10^6 cells, respectively. Ideal refers the ideal speedup; that is, when we double the number of processors, the total simulation time is exactly halved.

TABLE VII. Parallel performance of each stage of the simulation algorithm. The numbers on the left and right sides of “/” refer to meshes with 12.4 and 29.6×10^6 cells, respectively.

Number of processors	Mesh update (s)	Momentum prediction (s)	Solve the Poisson equation (s)	Solve turbulence equations (s)
48	59.66/222.2	37.13/85.7	73.37/219.65	31.31/71.25
96	36.87/129.55	19.31/49.45	38.67/125.27	15.15/38.54
192	22.43/70.39	8.81/24.58	24.77/70.39	6.67/18.38
384	15.67/43.08	4.63/13.73	26.27/49.01	3.28/9.1
768	10.19/29.56	2.26/6.69	23.65/31.94	1.52/4.29

This parallel simulation algorithm scales up to 768 processors for this computation, with problem sizes of over 12 and 29×10^6 cells. The parallel efficiency is over 50% when use 768 processors, which shows the potential to do higher resolution simulations using more processor cores.

ACKNOWLEDGMENTS

This work was partially supported by the National Natural Science Foundation of China (NSFC) (Nos. 62161160312 and 12071461) and Shenzhen Fundamental Research Program (No. RCYX20200714114735074).

AUTHOR DECLARATIONS

Conflict of Interest

The authors have no conflicts to disclose.

Author Contributions

Wei Chen: Simulation (equal); Methodology (equal); Software (equal); Writing – original draft (equal). **Hairong Zheng:** Conceptualization (equal); Project administration (equal). **Zhengzheng Yan:** Conceptualization (equal); Methodology (equal). **Rongliang Chen:** Conceptualization (equal); Methodology (equal); Writing – review & editing (equal); Supervision (equal).

DATA AVAILABILITY

The data that support the findings of this study are available from the corresponding author upon reasonable request.

REFERENCES

- ¹P. J. Wolfson, “The development and use of extracorporeal membrane oxygenation in neonates,” *Ann. Thorac. Surg.* **76**, S2224–S2229 (2003).
- ²B. Feiger, A. Adebiyi, and A. Randles, “Multiscale modeling of blood flow to assess neurological complications in patients supported by venoarterial extracorporeal membrane oxygenation,” *Comput. Biol. Med.* **129**, 104155 (2021).
- ³R. A. Malinauskas, P. Hariharan, S. W. Day, L. H. Herbertson, M. Buesen, U. Steinseifer, K. I. Aycock, B. C. Good, S. Deutsch, K. B. Manning *et al.*, “FDA benchmark medical device flow models for CFD validation,” *ASAIO J.* **63**, 150–160 (2017).
- ⁴M. E. Taskin, T. Zhang, K. H. Fraser, B. P. Griffith, and Z. J. Wu, “Design optimization of a wearable artificial pump-lung device with computational modeling,” *J. Med. Devices* **6**, 31009 (2012).
- ⁵P. Puentener, M. Schuck, and J. W. Kolar, “CFD assisted evaluation of in vitro experiments on bearingless blood pumps,” *IEEE Trans. Biomed. Eng.* **68**, 1370–1378 (2021).
- ⁶P. Puentener, M. Schuck, and J. W. Kolar, “The influence of impeller geometries on hemolysis in bearingless centrifugal pumps,” *IEEE Open J. Eng. Med. Biol.* **1**, 316–323 (2020).
- ⁷M. Fu, G. Liu, W. Wang, B. Gao, B. Ji, Y. Chang, and Y. Liu, “Hemodynamic evaluation and in vitro hemolysis evaluation of a novel centrifugal pump for extracorporeal membrane oxygenation,” *Ann. Transl. Med.* **9**, 679 (2021).

- ⁸W. Yang, S. Peng, W. Xiao, Y. Hu, H. Wu, and M. Li, "CFD-based flow channel optimization and performance prediction for a conical axial maglev blood pump," *Sensors* **22**, 1642 (2022).
- ⁹Y. Liu, N. Xie, Y. Tang, and Y. Zhang, "Investigation of hemocompatibility and vortical structures for a centrifugal blood pump based on large-eddy simulation," *Phys. Fluids* **34**, 115111 (2022).
- ¹⁰B. C. Good and K. B. Manning, "Computational modeling of the Food and Drug Administration's benchmark centrifugal blood pump," *Artif. Organs* **44**, E263–E276 (2020).
- ¹¹B. Ghadimi, A. Nejat, S. A. Nourbakhsh, and N. Naderi, "Shape optimization of a centrifugal blood pump by coupling CFD with metamodel-assisted genetic algorithm," *J. Artif. Organs* **22**, 29–36 (2019).
- ¹²M. E. Taskin, K. H. Fraser, T. Zhang, C. Wu, B. P. Griffith, and Z. J. Wu, "Evaluation of Eulerian and Lagrangian models for hemolysis estimation," *ASAIO J.* **58**, 363–372 (2012).
- ¹³J. Zhang, T. D. Nolan, T. Zhang, B. P. Griffith, and Z. J. Wu, "Characterization of membrane blood oxygenation devices using computational fluid dynamics," *J. Membr. Sci.* **288**, 268–279 (2007).
- ¹⁴M. E. Taskin, K. H. Fraser, T. Zhang, B. P. Griffith, and Z. J. Wu, "Micro-scale modeling of flow and oxygen transfer in hollow-fiber membrane bundle," *J. Membr. Sci.* **362**, 172–183 (2010).
- ¹⁵A. Kaesler, M. Rosen, T. Schmitz-Rode, U. Steinseifer, and J. Arens, "Computational modeling of oxygen transfer in artificial lungs," *Artif. Organs* **42**, 786–799 (2018).
- ¹⁶S. P. Madhani, B. J. Frankowski, and W. J. Federspiel, "Fiber bundle design for an integrated wearable artificial lung," *ASAIO J.* **63**, 631 (2017).
- ¹⁷M. E. Taskin, T. Zhang, C. Wu, B. P. Griffith, and Z. J. Wu, "CFD assisted design of a wearable artificial pump lung device," in *2008 ASME IMECE* (ASME, 2008), pp. 187–193.
- ¹⁸Z. J. Wu, M. E. Taskin, T. Zhang, K. H. Fraser, and B. P. Griffith, "Computational model-based design of a wearable artificial pump-lung for cardiopulmonary/respiratory support," *Artif. Organs* **36**, 387–399 (2012).
- ¹⁹J. Zhang, M. E. Taskin, A. Koert, T. Zhang, B. Gellman, K. A. Dasse, R. J. Gilbert, B. P. Griffith, and Z. J. Wu, "Computational design and in vitro characterization of an integrated maglev pump-oxygenator," *Artif. Organs* **33**, 805–817 (2009).
- ²⁰T. Zhang, G. Cheng, A. Koert, J. Zhang, B. Gellman, G. K. Yankey, A. Satpute, K. A. Dasse, R. J. Gilbert, B. P. Griffith *et al.*, "Functional and biocompatibility performances of an integrated maglev pump-oxygenator," *Artif. Organs* **33**, 36–45 (2009).
- ²¹S. P. Madhani, B. J. Frankowski, G. W. Burgreen, J. F. Antaki, R. Kormos, J. D'Cunha, and W. J. Federspiel, "In vitro and in vivo evaluation of a novel integrated wearable artificial lung," *J. Heart. Lung. Transplant.* **36**, 806–811 (2017).
- ²²S. P. Madhani, B. J. Frankowski, S.-H. Ye, G. W. Burgreen, W. R. Wagner, R. Kormos, J. D'Cunha, and W. J. Federspiel, "In vivo 5-day animal studies of a compact, wearable pumping artificial lung," *ASAIO J.* **65**, 94 (2019).
- ²³S. P. Madhani, A. G. May, B. J. Frankowski, G. W. Burgreen, and W. J. Federspiel, "Blood recirculation enhances oxygenation efficiency of artificial lungs," *ASAIO J.* **66**, 565–570 (2020).
- ²⁴D. Han, A. Shah, M. A. Awad, Z. J. Wu, and B. P. Griffith, "Development of an ambulatory extracorporeal membrane oxygenation system: From concept to clinical use," *Appl. Eng. Sci.* **10**, 100093 (2022).
- ²⁵LivaNova PLC, see <https://www.livanova.com/en-us/home/cardiopulmonary/heart-lung-equipment/revolution> for "Heart-lung equipment revolution" (2020).
- ²⁶D. Han, J. L. Leibowitz, L. Han, S. Wang, G. He, B. P. Griffith, and Z. J. Wu, "Computational fluid dynamics analysis and experimental hemolytic performance of three clinical centrifugal blood pumps: Revolution, rotaflow and centrimag," *Med. Novel Technol. Devices* **15**, 100153 (2022).
- ²⁷Z. Chen, S. K. Jena, G. A. Giridharan, S. C. Koenig, M. S. Slaughter, B. P. Griffith, and Z. J. Wu, "Flow features and device-induced blood trauma in CFVADs under a pulsatile blood flow condition: A CFD comparative study," *Int. J. Numer. Methods Biomed. Eng.* **34**, e2924 (2018).
- ²⁸M. E. Taskin, K. H. Fraser, T. Zhang, B. Gellman, A. Fleischli, K. A. Dasse, B. P. Griffith, and Z. J. Wu, "Computational characterization of flow and hemolytic performance of the ultramag blood pump for circulatory support," *Artif. Organs* **34**, 1099–1113 (2010).
- ²⁹C. S. Semenzin, "Determination of centrifugal blood pump characteristics using CFD and experimental analysis," Ph.D. thesis (Griffith University, 2020).
- ³⁰B. Thamsen, B. Blümel, J. Schaller, C. O. Paschereit, K. Affeld, L. Goubergrits, and U. Kertzscher, "Numerical analysis of blood damage potential of the HeartMate II and HeartWare HVAD rotary blood pumps," *Artif. Organs* **39**, 651–659 (2015).
- ³¹M. L. Heck, A. Yen, T. A. Snyder, E. A. O'Rear, and D. V. Papavassiliou, "Flow-field simulations and hemolysis estimates for the food and drug administration critical path initiative centrifugal blood pump," *Artif. Organs* **41**, E129–E140 (2017).
- ³²L. Könözy, *A New Hypothesis on the Anisotropic Reynolds Stress Tensor for Turbulent Flows*, Theoretical Background and Development of an Anisotropic Hybrid k-Omega Shear-Stress Transport/Stochastic Turbulence Model Vol. I (Springer, Cham, 2019).
- ³³F. R. Menter, "Two-equation eddy-viscosity turbulence models for engineering applications," *AIAA J.* **32**, 1598–1605 (1994).
- ³⁴G. Fancher, "Henry Darcy - engineer and benefactor of mankind," *J. Pet. Technol.* **8**, 12–14 (1956).
- ³⁵S. Whitaker, "Flow in porous media I: A theoretical derivation of Darcy's law," *Transp. Porous Media* **1**, 3–25 (1986).
- ³⁶B. Lai, J. L. Miskimins, and Y.-S. Wu, "Non-Darcy porous-media flow according to the Barree and Conway model: Laboratory and numerical-modeling studies," *SPE J.* **17**, 70–79 (2012).
- ³⁷A. J. E. V. Soares, "Numerical simulation of vegetated flows using RANS equations coupled with a porous media approach in OpenFOAM," Ph.D. thesis (Universidade NOVA de Lisboa, 2017).
- ³⁸F. Cimolin and M. Discacciati, "Navier–Stokes/Forchheimer models for filtration through porous media," *Appl. Numer. Math.* **72**, 205–224 (2013).
- ³⁹P. Forchheimer, "Wasserbewegung durch boden," *Z. Ver. Dtsch. Ing.* **45**, 1782–1788 (1901).
- ⁴⁰C. Soulaire and H. A. Tchelepi, "Micro-continuum approach for pore-scale simulation of subsurface processes," *Transp. Porous Media* **113**, 431–456 (2016).
- ⁴¹A. Pelosi, J. Sheriff, M. Stevanella, G. B. Fiore, D. Bluestein, and A. Redaelli, "Computational evaluation of the thrombogenic potential of a hollow-fiber oxygenator with integrated heat exchanger during extracorporeal circulation," *Biomech. Model. Mechanobiol.* **13**, 349–361 (2014).
- ⁴²A. Garon and M.-I. Farinas, "Fast three-dimensional numerical hemolysis approximation," *Artif. Organs* **28**, 1016–1025 (2004).
- ⁴³K. M. Saqr, "Wall shear stress in the Navier-Stokes equation: A commentary," *Comput. Biol. Med.* **106**, 82–83 (2019).
- ⁴⁴T. Zhang, M. E. Taskin, H.-B. Fang, A. Pampori, R. Jarvik, B. P. Griffith, and Z. J. Wu, "Study of flow-induced hemolysis using novel Couette-type blood-shearing devices," *Artif. Organs* **35**, 1180–1186 (2011).
- ⁴⁵H. Yu, S. Engel, G. Janiga, and D. Thévenin, "A review of hemolysis prediction models for computational fluid dynamics," *Artif. Organs* **41**, 603–621 (2017).
- ⁴⁶X.-K. Zhu and B. N. Leis, "Average shear stress yield criterion and its application to plastic collapse analysis of pipelines," *Int. J. Pressure Vessels Piping* **83**, 663–671 (2006).
- ⁴⁷H. Sundar, G. Biros, C. Burstedde, J. Rudi, O. Ghattas, and G. Stadler, "Parallel geometric-algebraic multigrid on unstructured forests of octrees," in *SC'12: Proceedings of the International Conference on High Performance Computing, Networking, Storage and Analysis* (IEEE, 2012), pp. 1–11.
- ⁴⁸Y. Deng, L. Zhang, D. Sun, and B. Yu, "Development of an efficient large time step unsteady solver for incompressible flows using the IDEAL algorithm in OpenFOAM," *J. Comput. Sci.* **61**, 101692 (2022).
- ⁴⁹H. Jasak, "Error analysis and estimation for the finite volume method with applications to fluid flows," Ph.D. thesis (University of London, 1996).
- ⁵⁰P. J. Roache, "Perspective: A method for uniform reporting of grid refinement studies," *J. Fluids Eng.* **116**, 405–413 (1994).
- ⁵¹F. M. Sakri, M. M. Ali, and S. S. Salim, "Computational investigations and grid refinement study of 3D transient flow in a cylindrical tank using OpenFOAM," *IOP Conf. Ser.: Mater. Sci. Eng.* **152**, 012058 (2016).

- ⁵²D. C. Wilcox, *Turbulence Modeling for CFD* (DCW Industries, La Canada, California, 1998), Vol. 2.
- ⁵³See <https://www.openfoam.com/documentation/guides/latest/doc/guide-fof-field-wallShearStress.html> for “OpenFOAM: User Guide” (2022).
- ⁵⁴J. Zhang, B. Gellman, A. Koert, K. A. Dasse, R. J. Gilbert, B. P. Griffith, and Z. J. Wu, “Computational and experimental evaluation of the fluid dynamics and hemocompatibility of the centrimag blood pump,” *Artif. Organs* **30**, 168–177 (2006).
- ⁵⁵Z. J. Wu, B. Gellman, T. Zhang, M. E. Taskin, K. A. Dasse, and B. P. Griffith, “Computational fluid dynamics and experimental characterization of the pediatric pump-lung,” *Cardiovasc. Eng. Technol.* **2**, 276–287 (2011).